AGU PUBLICATIONS

JGR

Journal of Geophysical Research: Space Physics

RESEARCH ARTICLE
10.1002/2015JA021604

Effects of conductivity perturbations in time-dependent global electric circuit model

Jaroslav Jánský[1] and Victor P. Pasko[1]

[1] Communications and Space Sciences Laboratory, Department of Electrical Engineering, Penn State University, University Park, PA, USA

Key Points:
- Reduced conductivity in thundercloud and presence of mountain are studied
- Ionospheric potential in case of extreme gamma ray burst is quantified
- Equivalent circuit models are valid for horizontal resolution of 20 km and more

Correspondence to:
J. Jánský,
jxj21@psu.edu

Citation:
Jánský, J., and V. P. Pasko (2015), Effects of conductivity perturbations in time-dependent global electric circuit model, *J. Geophys. Res. Space Physics*, *120*, 10,654–10,668, doi:10.1002/2015JA021604.

Received 21 JUN 2015
Accepted 5 NOV 2015
Accepted article online 9 NOV 2015
Published online 4 DEC 2015

Abstract This paper contributes to the understanding of the influence of conductivity perturbations on the ionospheric potential in the Earth's global electric circuit (GEC). The conductivity perturbations appearing in the middle atmosphere produced by γ ray bursts from magnetars are studied first. The transient response of the ionospheric potential is modeled in this case, and timescales of interest are identified (0.01–10s). In this case modification of ionospheric potential is small. Additionally, the principal effects of topography and reduction of conductivity inside the thundercloud are studied. Both of these factors effectively increase the ionospheric potential for a classic source in the GEC represented by a current dipole leading to formation of two main charge centers of the thunderstorm. On the other hand, for GEC including topography and conductivity reduction in thunderclouds the contribution of sequence of negative cloud-to-ground lightning discharges to the ionospheric potential is decreased. Simulation results show a very good agreement with equivalent circuit models for conductivity perturbations with horizontal dimensions exceeding 20 km.

1. Introduction

Ionospheric potential, defined as the difference between the potential of the Earth and the potential of a sufficiently high upper atmospheric region, is found to be an important quantity, which can serve as a global indicator relating the state of global electric circuit (GEC) to the planetary climate [*Williams and Mareev*, 2014, section 10]. Recently, *Kalinin et al.* [2014] presented a mathematical formulation relating ionospheric potential to source currents in the atmosphere (e.g., due to a current system leading to formation of two main charge centers of the thunderstorm). The formulation allows to obtain analytical solutions for special cases, like horizontally independent conductivity.

The conductivity perturbations of the atmosphere, including horizontal variations, are recognized as an important component influencing GEC [*Zhou and Tinsley*, 2010; *Rycroft and Harrison*, 2012; *Williams and Mareev*, 2014]. A representative example of such perturbations is a reduction of conductivity inside the thundercloud [e.g., *Rycroft et al.*, 2007]. Other examples of conductivity perturbations include those produced by ionizing radiation associated with powerful γ ray bursts. The quasi-steady nature of cosmic ray ionization under normal conditions lends considerable stability to the medium of GEC [*Williams and Mareev*, 2014, section 14]. Departures from this steady condition, however, can and do occur. Extraordinary fluxes of hard gamma radiation originating from magnetars were observed, e.g., on 27 August 1998 [*Price and Mushtak*, 2001] and on 27 December 2004 [*Inan et al.*, 2007]. The spatial variations related to the Earth's topography can also be considered as a modification of conductivity close to the Earth's surface. *Slyunyaev et al.* [2014] studied the influence of the large-scale conductivity inhomogeneities in the atmosphere on the GEC and in particular on the ionospheric potential. Under a restriction that the height of the atmosphere is much smaller than the horizontal scales of the distributions of the conductivity and the external current density, explicit formulae for the ionospheric potential were derived. The developed approximation was shown to be equivalent to that of classical models of atmospheric electricity in which the atmosphere is divided into two or more columns and is replaced by a simple equivalent electric circuit model (ECM) [*Makino and Ogawa*, 1984; *Tinsley and Zhou*, 2006; *Zhou and Tinsley*, 2010; *Rycroft et al.*, 2007; *Rycroft and Odzimek*, 2010]. The results following from the approximate theory were compared to those obtained from direct numerical simulation. It was found that the suggested approximation qualitatively accounts for the dependence of the ionospheric potential on the

parameters of the conductivity distribution, although the relative error may be significant, especially in the case of a substantial reduction of conductivity inside the thunderclouds.

Jánský and Pasko [2014] modeled charge balance and ionospheric potential dynamics in time-dependent GEC. It was shown that the complex time behavior of the GEC can be efficiently described using a solution corresponding to the impulse response of the system to the instantaneous input of a point charge. In particular, the impulse response (can be viewed as Green's function or fundamental solution) was used for description of constant current sources leading to formation of two main charges of thunderstorm and negative cloud-to-ground (−CG) lightning discharge. It was demonstrated that the time integral of ionospheric potential impulse response [*Jánský and Pasko*, 2014, Figure 6b] can be effectively used to determine the ionospheric potential in a steady state [*Jánský and Pasko*, 2014, equations (20) and (29)].

This paper contributes to the understanding of the influence of the conductivity perturbations on the ionospheric potential. First, the consistency of the two most recent approaches by *Kalinin et al.* [2014] and *Jánský and Pasko* [2014] is demonstrated for the case of horizontally independent conductivity in section 3.1. Then for special cases of horizontally dependent conductivity, which can be calculated by ECM, the comparison with time-dependent GEC model is constructed in section 3.2. The transient response of the ionospheric potential to the large-scale conductivity perturbations produced by γ ray bursts from magnetars [*Price and Mushtak*, 2001] is studied in section 4.1. The validity limits of the ECM are determined in terms of the horizontal dimension of the studied perturbations. The topography influence is discussed in section 4.2, and the influence of reduced conductivity inside the thunderclouds is discussed in section 4.3.

2. Numerical Model Formulation

We use a time-dependent axially symmetric spherical model of the electrical behavior of the global electric circuit described in *Jánský and Pasko* [2014]. Briefly, the model is based on the continuity equation for charge density ρ:

$$\frac{\partial \rho}{\partial t} + \vec{\nabla} \cdot (\sigma \vec{E}) = S_{\mathrm{cur}}\,, \tag{1}$$

and Poisson's equation for the electric potential ϕ:

$$\vec{\nabla}^2 \phi = -\rho/\varepsilon_0\,, \tag{2}$$

where $\vec{E} = -\vec{\nabla}\phi$ is the electric field, σ is the conductivity of the media, S_{cur} is the current source term, and ε_0 is the permittivity of free space. We will refer in this work to this type of model as CPM, as this model is based on continuity and Poisson's equations.

The schematics of the simulation domain is shown in Figure 1a. The model employs a spherical coordinate system $(r,\ \theta,\ \varphi)$ with the origin positioned at the center of the Earth at $r = 0$ km. The model domain includes the highly conducting Earth, a relatively thin layer representing the weakly conducting atmosphere and the ionosphere, and a large free space domain bounded by a remote spherical shell representing the physical condition of zero potential $\phi = 0$ at infinity. The radius of the remote spherical shell is $r_{\mathrm{out}} = 1322\, r_{\mathrm{Earth}} = 8.4\times10^6$ km, and the change in r_{out} with respect to previous work [*Jánský and Pasko*, 2014] is a consequence of mesh step exponential expansion with an increased factor of 1.15 with the intention of reducing the amount of points in radial direction. Equations (1) and (2) are discretized using a finite volume scheme on a structured mesh with the mesh refined in areas of interest to 1 km in radial direction and 0.5 km in horizontal direction.

To describe motion of charges inside the system, spatially variable conductivity is introduced. Inside the Earth the conductivity is set to $\sigma_{\mathrm{Earth}} = 10^{-6}\ \mathrm{S\,m^{-1}}$. This conductivity is sufficiently high to allow evolution of charge inside the Earth on timescales faster than the times of ionospheric potential variation [*Jánský and Pasko*, 2014]. In the air above the Earth's surface the exponential approximation of the conductivity is used [*Dejnakarintra and Park*, 1974]:

$$\sigma(h) = 5\times10^{-14}\ \exp(h/l)\ \mathrm{S\,m^{-1}}, \tag{3}$$

where h is the altitude and $l = 6$ km is the altitude scaling distance. Then $r_{\mathrm{TIB}} = r_{\mathrm{Earth}} + h_{\mathrm{TIB}}$, where $h_{\mathrm{TIB}} = 140$ km, describes radial distance from the Earth's surface to the top of the model ionosphere. Above r_{TIB}, in the area considered as free space, the conductivity is set to zero. Zero conductivity of free space surrounding GEC keeps charge confined to GEC. The exponential conductivity profile is considered as a very good approximation under 70 km where ion conductivity prevails [*Dejnakarintra and Park*, 1974, Figure 4]. Above 70 km,

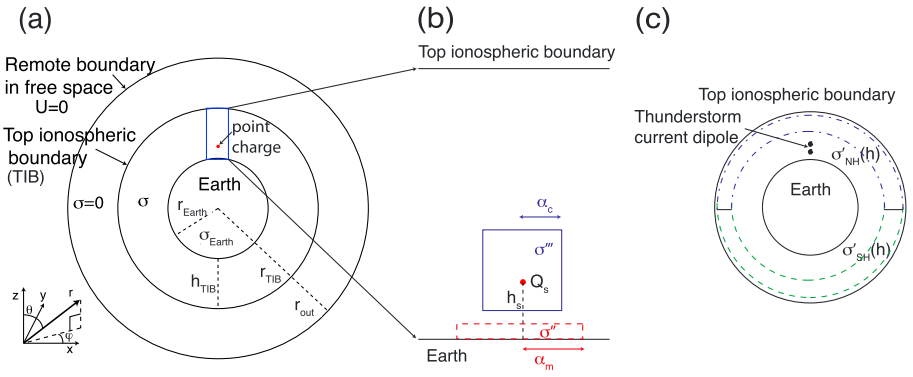

Figure 1. Schematics of the computational domain. (a) Full view of Earth, top ionospheric boundary, and zero-potential remote boundary (drawn not to scale). (b) Zoom-in view of the volume close to the axis $\theta = 0°$ where the initial point charge Q_s is introduced. The dashed line rectangle σ'' represents the modification of conductivity inside the cylindrically shaped model mountain. The solid line rectangle σ''' represents the reduction of conductivity inside the cylindrically shaped thundercloud. (c) The modification of conductivity above 20 km due to the γ ray burst. The quantity σ'_{NH} corresponds to conductivity perturbation in the Northern Hemisphere on the same side of the Earth as thunderstorm. The quantity σ'_{SH} corresponds to conductivity perturbation in the Southern Hemisphere on the opposite side of the Earth with respect to thunderstorm.

the electron conductivity is dominant and the total conductivity is increasing with increasing altitude and with shorter altitude scaling distance than 6 km and becomes anisotropic. This high conductivity together with various processes contribute to charge redistribution in the ionosphere [*Tzur and Roble*, 1985; *Stansbery et al.*, 1993]. *Tzur and Roble* [1985] indicated the importance of the equalization layer in spreading the current output from the thunderstorm and in maintaining global fair-weather conditions. The altitude 140 km of the top ionospheric boundary is chosen to provide sufficiently high conductivity so that the whole top ionospheric boundary will behave with very good accuracy as an equipotential layer. The higher altitude of the top ionospheric boundary is chosen, the higher accuracy of the equipotential layer is obtained. We emphasize the importance of accurate model representation of the highly conducting ionosphere for correct description of charge flow and redistribution in this system. Our high-altitude boundary captures principal dynamics of the real system by employing exponential conductivity profile and simple boundary conditions.

In Figures 1b and 1c the three model types of conductivity perturbations studied in the present work are introduced. The topography is studied using a single mountain on the Earth's surface as schematically shown in Figure 1b using dashed lines. The model mountain is represented by a cylindrical area with height 1.5 km, and its radius α_m is varied from 5 km to 20 km. The conductivity inside the mountain is set to be equal to the conductivity of Earth $\sigma'' = \sigma_{Earth}$. The source point charge Q_s is placed directly above the center of the mountain at altitude h_s. To take advantage of axial symmetry, the source charge is placed symmetrically around the axis $\theta = 0$ as schematically shown in Figure 1a. For model representation of the reduction of conductivity inside the thundercloud the conductivity is reduced to $\sigma''' = \sigma/20$ inside the cylindrical area with bottom boundary at 2.5 km and top boundary at 12.5 km. The radius of thundercloud α_c is again varied from 5 km to 20 km. Reduction of conductivity inside the clouds was estimated by measurements to be between 1/40 and 1/3 [*Pruppacher and Klett*, 1997, p. 802]. Recently, the model of *Zhou and Tinsley* [2010] calculated reduction of conductivity to be between 1/60 and 1/20 and the model of *Baumgaertner et al.* [2013] provided that the reduction can be even 2 orders of magnitude. However, the reduction of conductivity inside the thundercloud can be different due to electrification processes. The effect of reduction of conductivity inside the thundercloud on ionospheric potential created from a thundercloud current dipole was recently studied by *Slyunyaev et al.* [2014, Figure 5]. In our work the reduction of conductivity by a factor of 20 is used as a representative value. The source point charge Q_s is again placed on the axis $\theta = 0$, which coincides with the axis of symmetry of the thundercloud.

The conductivity σ' representing the modification at high altitudes due to the ionizing radiation from very intense γ ray burst is shown in Figure 1c. *Inan et al.* [2007] calculated conductivity modification due to the magnetar SGR 1806-20, and in this case the conductivity is increased by approximately 1 order of magnitude in the range of altitudes from 20 to 40 km and then relaxes to initial state. The conductivity perturbation appears above half of the Earth facing γ ray burst. In the present work the effect of γ ray burst on the contribution of a

single thunderstorm to GEC is studied. A thunderstorm is modeled as a current dipole at $\theta = 0$, and conductivity perturbation is applied either in the Northern Hemisphere (same as the thunderstorm) and denoted as σ'_{NH} for $0 < \theta < \pi/2$ or in the Southern (opposite) Hemisphere and denoted as σ'_{SH} for $\pi/2 < \theta < \pi$. The effect of high-altitude conductivity perturbation on ionospheric potential is small [*Slyunyaev et al.*, 2014], and therefore, we exaggerate the perturbation by assuming that $\sigma'_{NH} = \sigma'_{SH} = 10\,\sigma$ above the altitude 20 km are introduced instantaneously and remain constant in time. We then investigate the characteristic timescales and magnitudes of the ionospheric potential change.

The ionospheric potential U_{IE} is defined as a difference between average potential on the top ionospheric boundary and average potential on the Earth:

$$U_{IE} = \frac{\oint_{TIB} \phi \, dS}{S_{TIB}} - \frac{\oint_{Earth} \phi \, dS}{S_{Earth}}, \tag{4}$$

where surface integrals are calculated over the top ionospheric boundary and the Earth's surface, with areas S_{TIB} and S_{Earth}, respectively. We emphasize that due to their high conductivity both boundaries maintain equipotential properties with very good accuracy. Note that we denote U as a potential difference, while ϕ stands for potential at a given position.

3. Analytical Theory

3.1. Horizontally Homogeneous Conductivity

In this section we develop a relation of the ionospheric potential to the source current and conductivity profile/resistance for the case of horizontally independent conductivity, extending the approach of impulse response introduced in *Jánský and Pasko* [2014]. The resulting formulae are consistent with the results published recently by *Kalinin et al.* [2014].

Jánský and Pasko [2014] showed that for constant conductivity in time, the time behavior of the GEC can be efficiently described using a solution corresponding to the impulse response of the system to the instantaneous input of a point charge—the evolution of a linear system after a short input signal is called impulse response in signal processing [*Lyons*, 1997, p. 165]. Charge transfer processes in the atmosphere, which can be approximated by source current dipole $\pm I_s$ (typically leading to the formation of two main charge centers of thunderstorm), can be reconstructed as a linear combination of solutions for two monopoles. It was demonstrated that the time integral from $\tau = 0$ to infinity of ionospheric potential impulse response $U^{IR}_{IE}(h, \tau)$ to the instantaneous input of point unit charge at altitude h determines the ionospheric potential in steady state U_{IE} [*Jánský and Pasko*, 2014, equation (19)]:

$$U_{IE} = I_s \left[\int_0^\infty U^{IR}_{IE}(h_1, \tau)\, d\tau - \int_0^\infty U^{IR}_{IE}(h_2, \tau)\, d\tau \right], \tag{5}$$

where point charges are placed at altitude h_1 corresponding to the top positive charge and h_2 corresponding to the bottom negative charge. Using this approach, only one distribution providing information about altitude dependence of the time integral of ionospheric potential impulse response [*Jánský and Pasko*, 2014, Figure 6b] is necessary for the evaluation of steady state ionospheric potential of all possible multipole configurations for a given conductivity profile.

We now develop an analytical formulation for ionospheric potential U_{IE} for the case of horizontally independent conductivity by following the approaches of *Browning et al.* [1987] and *Kalinin et al.* [2014]. The ionospheric potential is independent of point charge horizontal coordinates φ and θ as both conductivity and average potential difference between the top ionospheric boundary and the Earth are the same for any horizontal coordinates [*Jánský and Pasko*, 2014, Appendix]. The point charge Q at altitude h_Q gives then the same ionospheric potential as the same charge Q distributed homogeneously on the spherical surface at the same altitude h_Q. Therefore, we solve the problem only in one-dimensional radial coordinate, assuming spherical symmetry.

We transform the continuity equation (1) and Poisson's equation (2) to the following form as a function only of radial coordinate and time:

$$\frac{\partial}{r^2\, \partial r} \left[r^2 \left(\sigma E + \frac{\varepsilon_0 \partial E}{\partial t} + J_s \right) \right] = 0, \tag{6}$$

where J_s is the charge separation current density, which is a different representation of the source current S_{cur} from equation (1) and they are linked through a relationship $S_{cur} = -\vec{\nabla} \cdot \vec{J}_s$. We multiply equation (6) by r^2 and integrate from $r = 0$ to arbitrary altitude h and obtain

$$\left[r^2 \left(\sigma E + \frac{\varepsilon_0 \partial E}{\partial t} + J_s \right) \right]_{r=0}^{r=h} = 0 \,. \tag{7}$$

It is important to note that there is no inner boundary in our model and we integrate from $r = 0$. The model of *Kalinin et al.* [2014] can follow the analogical derivation due to the addition of boundary condition on the inner surface of their domain [*Kalinin et al.*, 2014, equation (11)]. The lower bound of equation (7) at $r = 0$ is zero. The rest of equation (7) at $r = h$ can then be divided by h^2, and we therefore can write for any altitude h

$$\sigma E + \frac{\varepsilon_0 \partial E}{\partial t} + J_s = 0 \,. \tag{8}$$

This is the first-order ordinary differential equation leading to the following solution:

$$E(h,t) = E(h,t=0)\, \exp\left(-\frac{\sigma(h)}{\varepsilon_0} t \right) - \int_0^t \frac{J_s(h,\tau)}{\varepsilon_0} \exp\left(-\frac{\sigma(h)}{\varepsilon_0} (t-\tau) \right) \mathrm{d}\tau \,. \tag{9}$$

The first term on the right-hand side of equation (9) agrees with the solution reported by *Browning et al.* [1987, equation (4.9)]. To obtain the ionospheric potential U_{IE}, we integrate the electric field from the Earth to the top ionospheric boundary:

$$U_{IE}(t) = -\int_0^{h_{TIB}} \left[E(h,t=0) \exp\left(-\frac{\sigma(h)}{\varepsilon_0} t \right) - \int_0^t \frac{J_s(h,\tau)}{\varepsilon_0} \exp\left(-\frac{\sigma(h)}{\varepsilon_0} (t-\tau) \right) \mathrm{d}\tau \right] \mathrm{d}h \,. \tag{10}$$

This equation is in agreement with *Kalinin et al.* [2014, equation (33)]. We have derived it here in SI units, and the one-dimensionality of our approach is equivalent to averaging over the polar and azimuthal coordinates in *Kalinin et al.* [2014, section 6]. It is important to note that different boundary conditions of models in the present work and the work of *Kalinin et al.* [2014] have no influence on ionospheric potential results.

After solving the ionospheric potential in one dimension for arbitrary charge separation current density J_s, we will analyze the specific problem of instantaneously inputed charge Q distributed on a spherical surface at altitude h_Q. The input of charge Q can be represented as $Q\,\delta(h - h_Q)\,\delta(t) = S_{cur} = -\vec{\nabla} \cdot \vec{J}_s$, where δ represents delta function. This leads to charge separation current $J_s = 0$ for time $t > 0$ in equation (10). Then the ionospheric potential $U_{IE}(t)$ depends only on initial electric field $E(h, t = 0)$. The spherical charge Q at altitude h_Q creates electric field $E(h, t = 0)$:

$$\begin{aligned} E(h,t=0) &= 0 \,, \quad h < h_Q \,, \\ E(h,t=0) &= \frac{Q}{4\pi\varepsilon_0 (r_{Earth} + h)^2} \,, \quad h \geq h_Q \,. \end{aligned} \tag{11}$$

We now evaluate the quantity $M_{IE}^{IR}(h_Q) = \int_0^\infty U_{IE}^{IR}(h_Q, t)\,\mathrm{d}t$, time integral of impulse response of ionospheric potential $U_{IE}^{IR}(h_Q, t)$ to the instantaneous input of point unit charge at altitude h_Q. Note that point unit charge in a one-dimensional spherically symmetric problem is equivalent to the unit charge distributed on spherical surface at the same altitude. To obtain M_{IE}^{IR}, we integrate equation (10) in time. Having utilized also equation (11) for electric field, we derive the following relation:

$$\begin{aligned} -Q\, M_{IE}^{IR}(h_Q) &= -Q \int_0^\infty U_{IE}^{IR}(h_Q,t)\,\mathrm{d}t = -\int_0^\infty U_{IE}(Q,h_Q,t)\,\mathrm{d}t = \int_0^\infty \int_0^{h_{TIB}} E(h,t)\,\mathrm{d}h\,\mathrm{d}t \\ &= \int_{h_Q}^{h_{TIB}} \int_0^\infty \frac{Q}{4\pi\varepsilon_0 (r_{Earth}+h)^2} \exp\left(-\frac{\sigma(h)}{\varepsilon_0} t \right) \mathrm{d}t\,\mathrm{d}h \\ &= \int_{h_Q}^{h_{TIB}} \frac{Q}{4\pi (r_{Earth}+h)^2 \sigma(h)} \mathrm{d}h = Q\, R_{Q-TIB} \,, \end{aligned} \tag{12}$$

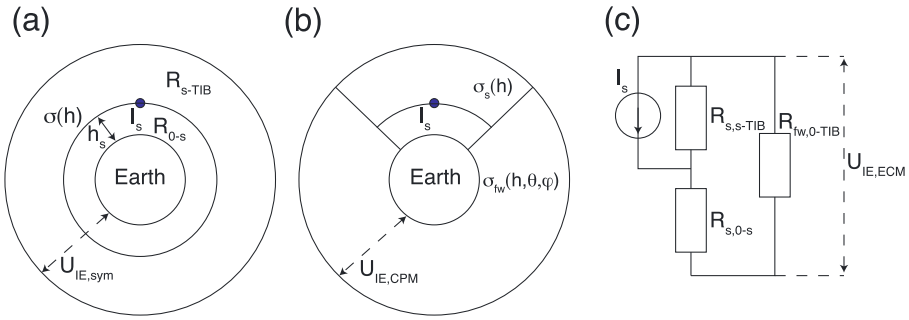

Figure 2. Schematics of the electrical quantities in GEC with point source current I_s placed at altitude h_s. (a) GEC for horizontally independent conductivity $\sigma(h)$. The quantities R_{s-TIB} and R_{0-s} are resistance of the entire atmosphere above the altitude of source and resistance under the altitude of source, respectively. The quantity $U_{IE,sym}$ denotes ionospheric potential. (b) A model case with horizontally independent conductivity $\sigma_s(h)$ only in the volume close to the source. The conductivity elsewhere $\sigma_{fw}(h,\theta,\varphi)$ can be horizontally dependent. The quantity $U_{IE,CPM}$ denotes ionospheric potential calculated using CPM. (c) Equivalent circuit, where the source current monopole is represented by current source I_s transferring the charge from the top boundary to the altitude of the monopole. The quantities $R_{s,s-TIB}$ and $R_{s,0-s}$ are resistances in the source column above and under the source, respectively, and $R_{fw,0-TIB}$ corresponds to the fair-weather resistance. The quantity $U_{IE,ECM}$ denotes ionospheric potential calculated using ECM.

where $U_{IE}(Q, h_Q, t)$ is ionospheric potential obtained from equation (10) and for a given spherically symmetric problem is a function of charge Q, charge altitude h_Q, and time t. Part of the integral on the last line of equation (12) corresponds to the resistance and is denoted R_{Q-TIB}. For horizontally independent conductivity the integral formulation of resistance is equal to the actual resistance, which would be obtained from Ohm's law by applying constant potential difference between the top ionospheric boundary and the Earth and measuring the current flowing between them. For horizontally dependent conductivity cases the resistances will be different due to the presence of horizontal currents. We can conclude that $-M_{IE}^{IR}$ is equal to resistance R_{Q-TIB} of the atmosphere between the altitude of input charge h_Q and the top ionospheric boundary. All resistances R in this paper will be evaluated from the integral formulation. Note that the R represents resistance while r represents radial coordinate. Note also that the derivations in section 3.1 are performed for an arbitrary (but horizontally independent) conductivity profile and no constraints related to exponential conductivity profile were used.

Equation (5) provides a link between steady state ionospheric potential U_{IE}, source current I_s, and time integral of ionospheric potential impulse response M_{IE}^{IR}. After transforming M_{IE}^{IR} into resistances based on equation (12), we obtain an equation showing that the ionospheric potential depends only on resistance between the altitudes of current sources in the current dipole:

$$U_{IE} = I_s\,(-R_{TP-TIB}) - I_s\,(-R_{BN-TIB}) = I_s\,R_{BN-TP}\,. \tag{13}$$

where the resistance above the bottom negative charge is R_{BN-TIB}, the resistance above the top positive charge is R_{TP-TIB}, and the resistance between charges is $R_{BN-TP} = R_{BN-TIB} - R_{TP-TIB}$. Equation (31) in *Kalinin et al.* [2014] relating the ionospheric potential in steady state with conductivity and source current flux density is consistent with this result.

Equation (5) is for the dipole current source, but as it has been mentioned above it represents a linear combination of solutions for two monopoles. It is therefore only necessary to analyze monopole sources, and other solutions can be obtained by simple addition/superposition. Schematics of such a setup with horizontally independent conductivity $\sigma(h)$ is shown in Figure 2a. The resistance above the source current I_s and over the entire atmosphere is labeled as R_{s-TIB} and the resistance under as R_{0-s}. Then ionospheric potential $U_{IE,sym}$ ("sym" stands for symmetric as in this case nothing depends on the polar and azimuthal coordinates) can be precisely evaluated:

$$U_{IE,sym} = I_s\,M_{IE}^{IR} = I_s\,(-R_{s-TIB})\,. \tag{14}$$

It is important to note that the ionospheric potential due to the positive current monopole is negative contrary to the positive ionospheric potential due to the dipole with top positive and bottom negative charges

described by equation (13). It is because the bottom negative monopole in the dipole contributes more to the ionospheric potential than the top positive ($R_{BN-TIB} > R_{TP-TIB}$). For a more discussion on negative ionospheric potential due to the positive current monopole and how it relates to results for a current monopole from the classical model of *Holzer and Saxon* [1952] with grounded Earth as boundary condition, see *Jánský and Pasko* [2014, section 3.2].

3.2. Conductivity With Horizontal Variations

All the calculations in section 3.1 were performed under assumption of horizontally independent (spherically symmetric) conductivity. The horizontal variations in conductivity in GEC are incorporated in numerous models using equivalent circuit models (ECMs) [*Makino and Ogawa*, 1984; *Tinsley and Zhou*, 2006; *Zhou and Tinsley*, 2010; *Rycroft et al.*, 2007; *Rycroft and Odzimek*, 2010]. Their horizontal mesh resolution is usually hundreds of kilometers corresponding to resolution of available input data (conductivity and thunderstorm distributions). A full three-dimensional model [*Bayona et al.*, 2015], based on coupling of the continuity equation and Poisson's equation (denoted as CPM in section 2), incorporates the best horizontal resolution of 40 km. Recently, *Slyunyaev et al.* [2014] compared ECM with results obtained from steady state CPM and found very good agreement under restriction that the height of the atmosphere is much smaller than the horizontal scales of the distributions of the conductivity and the external current density. *Slyunyaev et al.* [2014] showed also a disagreement between ECM and CPM for horizontal scales of 5 km. As part of our present work, we present a comparison between ECM results and CPM results for horizontal scales between 5 km and hundreds of kilometers. This is motivated by the need to establish a quantitative value when the two models agree or disagree. *Baumgaertner et al.* [2014] already described the role of clouds, and conductivity perturbations of horizontal scales from several to hundreds of kilometers, in the fair-weather part of GEC. They modify the global resistance of GEC. The present work focuses on analysis of conductivity perturbations around sources, as they modify also the current outflow from sources to GEC.

The studied horizontal scales are small relative to GEC dimensions and therefore very fine mesh resolution is required for description of CPM model. Then the solution for the full GEC discretized with such resolution would be extremely time-consuming. We introduce only one region with conductivity profile around the source $\sigma_s(h)$ and use a high-resolution mesh only in the surrounding volume. The schematics of CPM and ECM are shown in Figures 2b and 2c, respectively. If the conductivity perturbation is located outside of the source region, it can be included in the fair-weather part of the domain, which is described by conductivity $\sigma_{fw}(h, \theta, \varphi)$. The σ_{fw} is considered as a function of horizontal coordinates θ and φ as it can be composed of several domains of sufficiently large horizontal size with horizontally independent conductivity [see *Slyunyaev et al.*, 2014, Figure 1].

Next we solve the ECM model schematically shown in Figure 2c. First, we explain how each component of the circuit is calculated. The resistances in the source volume $R_{s,s-TIB}$ and $R_{s,0-s}$ in ECM are defined from altitude integration of conductivity σ_s. The equation for resistance above the source is

$$R_{s,s-TIB} = \int_{h_s}^{h_{TIB}} \frac{dh}{(r_{Earth} + h)^2 \, \sigma_s \, \Omega'} , \tag{15}$$

where Ω' in units of steradian (sr) corresponds to the solid angle subtended by volume covered by σ_s, which would integrate to 4π over the whole Earth. The resistance under the source $R_{s,0-s}$ is defined in a similar way with modified limits of integration from $h = 0$ to h_s. Later in the text the resistance of the whole source volume will also be used $R_{s,0-TIB} = R_{s,0-s} + R_{s,s-TIB}$. In case the fair-weather region is composed of one region of horizontally independent conductivity $\sigma_{fw}(h)$, the $R_{fw,0-TIB}$ is defined analogically to equation (15):

$$R_{fw,0-TIB} = \int_{0}^{h_{TIB}} \frac{dh}{(r_{Earth} + h)^2 \, \sigma_{fw} \, (4\pi - \Omega')} . \tag{16}$$

If the fair-weather region is composed of multiple domains with horizontally independent conductivity, each domain resistance is integrated separately and the final R_{fw} is obtained as their parallel connection.

Current source I_s in ECM is equivalent to the current dipole in CPM with I_s at altitude h_s and $-I_s$ at altitude h_{TIB}. The current monopole $-I_s$ at altitude h_{TIB} makes zero contribution to the ionospheric potential

[*Jánský and Pasko*, 2014, Appendix], and therefore, the current source in ECM represents purely the contribution of current monopole I_s at altitude h_s to the ionospheric potential.

All components of the circuit schematically shown in Figure 2c are now defined and explained. We proceed to the solution of the circuit using Kirchoff's current and voltage laws. The potential difference between the top ionospheric boundary and the Earth is then

$$U_{\mathrm{IE,ECM}} = I_s \frac{-R_{\mathrm{s,s-TIB}}}{R_{\mathrm{s,0-s}} + R_{\mathrm{s,s-TIB}} + R_{\mathrm{fw,0-TIB}}} R_{\mathrm{fw,0-TIB}} = I_s \frac{-R_{\mathrm{s,s-TIB}}}{R_{\mathrm{s,0-TIB}} + R_{\mathrm{fw,0-TIB}}} R_{\mathrm{fw,0-TIB}} . \tag{17}$$

Next we denote resistance of the atmosphere in ECM model $R_{\mathrm{atm}} = (1/R_{\mathrm{fw,0-TIB}} + 1/R_{\mathrm{s,0-TIB}})^{-1}$ as the parallel connection of source and fair-weather resistances. Then equation (17) can be rewritten into the following form:

$$U_{\mathrm{IE,ECM}} = I_s \frac{-R_{\mathrm{s,s-TIB}}}{R_{\mathrm{s,0-TIB}}} R_{\mathrm{atm}} . \tag{18}$$

Apart from viewing equation (18) as a solution of ECM in Figure 2c, it can be used for easy interpretation of results. Equation (18) can be viewed as Ohm's law for the whole atmosphere, and it states that potential difference $U_{\mathrm{IE,ECM}}$ creates downward directed current of value $I_s\, R_{\mathrm{s,s-TIB}}/R_{\mathrm{s,0-TIB}}$ flowing over the whole atmosphere. As the current in GEC in steady state is balanced, with the absence of potential difference $U_{\mathrm{IE,ECM}}$, the source I_s produces upward directed current of value $I_s\, R_{\mathrm{s,s-TIB}}/R_{\mathrm{s,0-TIB}}$ flowing mostly close to the source. In GEC, the two currents overlap. Therefore, the current flowing in ECM in Figure 2c depends on solid angle Ω'. Contrary, the potential difference $U_{\mathrm{IE,ECM}}$ evaluated from equation (18) has an interesting property that the ratio of resistances does not depend on volume covered by σ_s as the solid angle Ω' is the same for both resistances and is cancelled when the ratio is calculated; see equation (15). For any horizontal scales of hundreds of kilometers and less, the solid angle is small: $\Omega' < 10^{-3}$ sr. In this case the resistance of R_{atm} will stay almost constant and equal to $R_{\mathrm{fw,0-TIB}}$; however, based on equation (18), the ionospheric potential $U_{\mathrm{IE,ECM}}$ calculated from ECM is still independent of volume covered by σ_s.

To compare with CPM model, we calculate ionospheric potential $U_{\mathrm{IE,CPM}}$ using the model described in section 2 with conductivity distribution as shown in Figure 2b. The steady state ionospheric potential can be expressed as $U_{\mathrm{IE,CPM}} = I_s\, M_{\mathrm{IE}}^{\mathrm{IR}}$ even for horizontally dependent conductivity. The $M_{\mathrm{IE}}^{\mathrm{IR}}$ is therefore obtained from numerical simulation and compared with results from equation (18). The region with the conductivity σ_s is selected as cylinder with radius to be the same as the radius of the thundercloud or mountain described in section 2. The source current I_s is considered to be a point current that is located on the axis of symmetry of the region with conductivity σ_s.

4. Results and Discussion

4.1. Transient Conductivity Perturbations Due To γ Ray Bursts

In this section large-scale conductivity perturbations caused by very intense γ ray bursts are studied. The giant γ ray burst from magnetar SGR 1806-20 created a massive disturbance in the daytime lower ionosphere [*Inan et al.*, 2007]. The effects of this burst are approximated by a sudden change of conductivity by 1 order of magnitude above the altitude 20 km as described in section 2 and schematically shown in Figure 1c. The system involving a single thunderstorm source is studied. The thunderstorm is described as a current dipole placed at $\theta = 0$, with $I_s = 1$ A point current source located at altitude $h_{\mathrm{TP}} = 9.5$ km and -1 A point current source located at altitude $h_{\mathrm{BN}} = 4.5$ km. Modeling starts with obtaining a steady state solution for the system before perturbation is introduced. The time-dependent simulation is first run for 10^4 s with unperturbed exponential conductivity. The results are then used as initial conditions for the simulation with modified conductivity.

In Figure 3a the ionospheric potential evolution is plotted for a time interval after the γ ray burst produces perturbation of conductivity. The conductivity in this model case is increased in the Northern Hemisphere where model thundercloud source is placed. The conductivity is maintained unchanged in the Southern Hemisphere. The steady state solution before the perturbation is plotted using a dashed line. The logarithmic representation of time is used to identify important characteristic timescales. As the perturbation is introduced the ionospheric potential starts to be modified on a timescale of 10^{-2} s. The ionospheric potential increases and establishes new steady state on timescale of ~10 s. This timescale corresponds to the dielectric relaxation time (ε_0/σ) at altitudes between 10 km and 20 km.

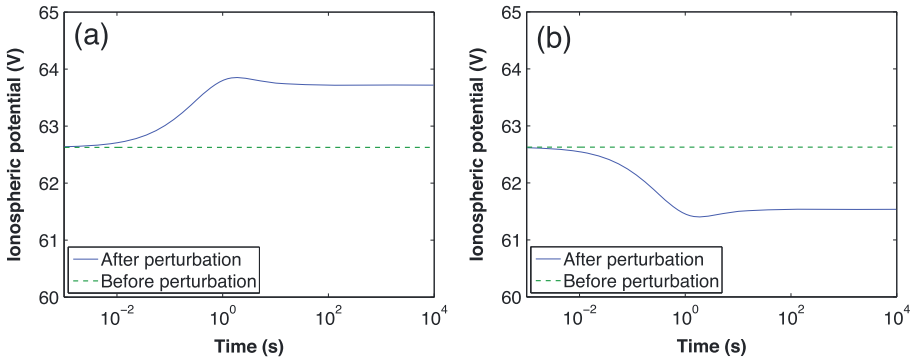

Figure 3. Time evolution of the contribution to ionospheric potential from a single thunderstorm represented by current dipole ±1 A. The contribution to ionospheric potential after conductivity perturbation caused by a γ ray burst is plotted with solid lines. (a) The case with thunderstorm on the same side of the Earth as conductivity perturbation. (b) The case with thunderstorm on the opposite side of the Earth with respect to the conductivity perturbation. Dashed lines correspond to the steady state contribution of thunderstorm to the ionospheric potential before perturbation.

In Figure 3b the ionospheric potential evolution after the perturbation is plotted in the case of the perturbation introduced in the opposite hemisphere. The ionospheric potential is decreasing in this case on the same timescales as in Figure 3a. It is interesting to note that if the whole atmosphere were ionized, the ionospheric potential would not change. This is because in symmetric case, the ionospheric potential is dependent only on the resistance between the altitude positions of source currents, which is not modified (see equation (13)). We remind the reader that conductivity perturbation is introduced only above 20 km (see section 2).

The change in steady state ionospheric potential is compared with results obtained from ECM. First, we define resistances in the ECM, and then we evaluate ionospheric potential using equation (17). It is important to note again that the choice of solid angle Ω' of the source column is not influencing the ionospheric potential as in equation (18); the solid angle Ω' enters in both resistances and is cancelled when the ratio of resistances is calculated. Then we chose for simplicity the ECM to be composed of two columns representing the Northern and Southern Hemispheres. The current source is added in the Northern Hemisphere column.

Then the resistances in the Northern and Southern Hemispheres without conductivity perturbation are obtained from integral:

$$R_{\mathrm{NH},0-\mathrm{TIB}} = R_{\mathrm{SH},0-\mathrm{TIB}} = \int_0^{h_{\mathrm{TIB}}} \frac{\mathrm{d}h}{2\,\pi\,(r_{\mathrm{Earth}}+h)^2\,\sigma(h)} = 469.6\,\Omega\,, \tag{19}$$

where the integral is evaluated over the solid angle 2π corresponding to half of the sphere and $\sigma(h)$ corresponds to the exponential conductivity profile. The resistances in the Northern and Southern Hemispheres with conductivity perturbation $\sigma' = 10\,\sigma$ above the altitude 20 km are obtained from integral:

$$R'_{\mathrm{NH},0-\mathrm{TIB}} = R'_{\mathrm{SH},0-\mathrm{TIB}} = \int_0^{h_{\mathrm{TIB}}} \frac{\mathrm{d}h}{2\,\pi\,(r_{\mathrm{Earth}}+h)^2\,\sigma'} = 454.6\,\Omega\,. \tag{20}$$

The resistances between the altitudes of bottom negative and top positive charge centers are the same for the cases with and without conductivity perturbation as they are located below the bottom boundary of the conductivity perturbation:

$$R_{\mathrm{NH,BN-TP}} = R'_{\mathrm{NH,BN-TP}} = \int_{h_{\mathrm{BN}}}^{h_{\mathrm{TP}}} \frac{\mathrm{d}h}{2\,\pi\,(r_{\mathrm{Earth}}+h)^2\,\sigma} = 125.4\,\Omega\,. \tag{21}$$

Equation (17) is for monopole contribution to ionospheric potential. To obtain the contribution of the dipole with current I_s at the altitude of top positive charge center h_{TP} and current $-I_s$ at the altitude of bottom

negative charge center h_{BN}, a linear combination of two monopoles is formed and the ionospheric potential is obtained in the following form:

$$U_{IE,ECM} = I_s \frac{-R_{s,TP-TIB}}{R_{s,0-TIB} + R_{fw,0-TIB}} R_{fw,0-TIB} + I_s \frac{R_{s,BN-TIB}}{R_{s,0-TIB} + R_{fw,0-TIB}} R_{fw,0-TIB} = I_s \frac{R_{s,BN-TP}}{R_{s,0-TIB} + R_{fw,0-TIB}} R_{fw,0-TIB}. \quad (22)$$

The ionospheric potential is evaluated from equation (22) before the perturbation assuming that the column with source is in the Northern Hemisphere and the fair-weather column corresponds to the Southern Hemisphere:

$$U_{IE,ECM} = I_s \frac{R_{NH,BN-TP}}{R_{NH,0-TIB} + R_{SH,0-TIB}} R_{SH,0-TIB} = 62.7\,\mathrm{V}. \quad (23)$$

The ionospheric potential after the perturbation in the Northern Hemisphere is then

$$U_{IE,ECM} = I_s \frac{R'_{NH,BN-TP}}{R'_{NH,0-TIB} + R_{SH,0-TIB}} R_{SH,0-TIB} = 63.7\,\mathrm{V}. \quad (24)$$

The ionospheric potential after the perturbation in the Southern Hemisphere is then

$$U_{IE,ECM} = I_s \frac{R_{NH,BN-TP}}{R_{NH,0-TIB} + R'_{SH,0-TIB}} R'_{SH,0-TIB} = 61.7\,\mathrm{V}. \quad (25)$$

The numerical simulation gives ionospheric potential 62.6 V before the perturbation, 63.7 V after the perturbation in the same hemisphere, and 61.5 V after the perturbation in the opposite hemisphere. The small, on the order of 1 V, differences due to perturbation (less than 2%) are caused by the small contribution of conductivity above 20 km to the total resistance of the atmosphere.

We can conclude based on the presented modeling that the transient response of ionospheric potential to the γ ray bursts occurs on timescales on the order of $10^{-2} - 10^{1}$ s. Modifications of the steady state ionospheric potential are small even for very intense γ ray bursts in agreement with *Slyunyaev et al.* [2014] as conductivity above 20 km has a small contribution to the total resistance. It is important to note that because conductivity perturbation remains constant in the present work, the results represent the upper limit of contribution of γ ray bursts to GEC. The effects of large-scale conductivity perturbation are very well reproduced by ECM, also in agreement with *Slyunyaev et al.* [2014].

4.2. Effects of Topography on Ionospheric Potential

In this section the influence of the topography in proximity of thunderstorms, or other current sources, on the ionospheric potential is studied. The comparison of results obtained from CPM and ECM, described in section 3.2, is the main motivation. For this comparison the exponential conductivity profile is used for transparency. Additional effects such as radon emanation and corona discharges from mountains are not considered in the simulation part of this section but are discussed based on the ECM.

The topography is introduced as the static conductivity enhancement close to the Earth's surface as shown schematically in Figure 1b. Contrary to the high-altitude conductivity perturbation studied in section 4.1, which has a small influence on resistance and correspondingly on ionospheric potential, the conductivity at low altitudes is low, and therefore, the contribution to the resistance is more significant. For example, if the Earth's surface is simply raised by 1 km in the entire opposite hemisphere to the thunderstorm from section 4.1, the ionospheric potential is decreased by 5.2 V from 62.7 V to 57.5 V (~8.3%).

This section focuses on examining the limits of validity of ECM for the calculation of ionospheric potential (see equation (18)). The schematics of conductivity perturbation is shown in Figure 1b. The point charge is introduced at $\theta = 0$ at altitude h_s, and conductivity is modified directly underneath the point charge in a cylindrical volume above the Earth's surface representing a flat mountain with height 1.5 km. The radius of mountain α_m is varied in the range from 5 to 20 km. We note that as demonstrated below for higher radii the agreement with ECM is excellent. The source altitude h_s is varied in the range of 0 to 15.5 km. The source altitude smaller than the mountain height is evaluated as representing charge transfer to Earth, similarly to CG discharges.

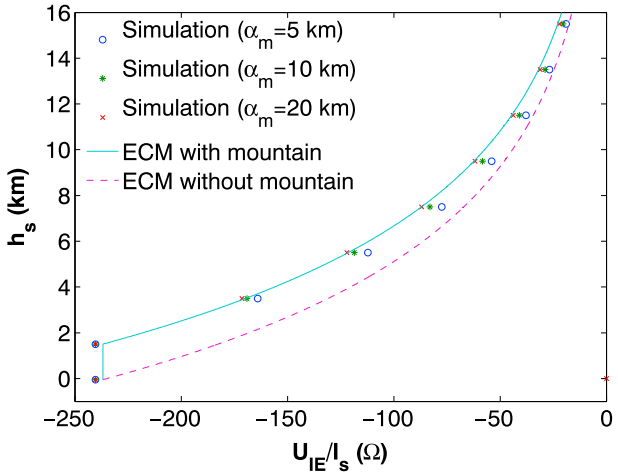

Figure 4. The CPM simulation results of U_{IE}/I_s as a function of source altitude h_s is plotted for three different mountain radii: $\alpha_m = 5$ km, 10 km, and 20 km. The mountain is 1.5 km high and has a cylindrical shape as shown in Figure 1b. The ECM results with mountain are obtained from equation (18) and are plotted using a solid line, and the ECM results for unperturbed exponential conductivity are plotted using a dashed line.

The results from CPM of ionospheric potential per unit current U_{IE}/I_s as a function of altitude for three different radii of the mountain are shown in Figure 4 along with ECM results obtained from equation (18). These data, as described in section 3, multiplied by source current will give the steady state ionospheric potential. Two ECM results are presented in Figure 4, one for a single mountain with perturbed conductivity σ'' labeled as "ECM with mountain" and the second without a mountain labeled as "ECM without mountain." We note that the ECM without mountain case corresponds to a situation with symmetric exponential conductivity where U_{IE}/I_s corresponds to $-R_{s-TIB}$. It is seen that for sources at low altitudes the ECM results with mountain agree very well with numerical simulation results for all considered mountain radii α_m. For higher altitudes of the sources and smaller mountain radius the U_{IE}/I_s approaches the ECM results without mountain, which means that the effect of a mountain disappears. The CPM simulation results of U_{IE}/I_s are slightly higher than the ECM results for low altitudes due to the time discretization error of about 1%. Using 10 times finer time resolution reduces it to less than 0.1%. An additional 1% error is found for values at altitude 0 km due to the finite thickness of the mesh layer (0.1 km) used to describe the Earth's surface layer containing the surface charge. It is important to note that within error all CPM simulation results are consistent and appear between two ECM curves.

We now apply the ECM and CPM results from Figure 4 for the case of source current dipole ($I_s = 1$ A placed at altitude $h_{TP} = 9.5$ km and $-I_s$ at $h_{BN} = 5.5$ km). In the case without mountain, equation (13) can be directly used to obtain $U_{IE} = 45.7$ V (for both CPM and ECM). In the case with mountain, the result from ECM has to be formed from a linear combination of two equations (18) for monopoles at h_{BN} and h_{TP}. The final form gives

$$U_{IE,ECM} = I_s \frac{R_{s,BN-TP}}{R_{s,0-TIB}} R_{atm} = 59.2\,\text{V}, \tag{26}$$

where $R_{s,BN-TP}$ and $R_{s,0-TIB}$ correspond to resistances in source column between the altitudes of bottom negative and top positive charges, and between the Earth and the top ionospheric boundary, respectively. The resistance $R_{s,0-TIB}$ is modified by the presence of a mountain, while resistance $R_{s,BN-TP}$ remains unchanged. The ratio of the resistances is $R_{s,BN-TP}/R_{s,0-TIB} = 0.252$. The quantity $R_{atm} = 234.8\,\Omega$ corresponds to the resistance of the whole atmosphere. The increase of ionospheric potential due to a single mountain of height 1.5 km directly underneath the source current is 29.5% based on ECM. *Hays and Roble* [1979] studied the influence of topography on GEC and investigated a test case when they moved all thunderstorm sources from land to ocean. This test case showed the effect of removal of elevated ground under the thunderstorms while keeping the fair-weather resistance effectively unchanged. They observed an increase of 19.3% in ionospheric potential by placing the thunderstorms above the land, which is in qualitative agreement with the results of the present work.

The ionospheric potential obtained from CPM simulation results is evaluated from Figure 4 as a linear combination of values U_{IE}/I_s obtained for monopoles at altitudes h_{BN} and h_{TP}:

$$U_{IE,CPM} = I_s \left[\frac{U_{IE}}{I_s}\left(h_{TP}\right) - \frac{U_{IE}}{I_s}\left(h_{BN}\right) \right] . \quad (27)$$

The ionospheric potential is then 60.323 V for the mountain with radius 20 km. The mountain with radius 10 km gives 60.322 V, and the mountain with radius 5 km gives 58.2 V. The differences between the ECM and the CPM are smaller than 2% for all radii.

It is observed that the presence of a mountain is increasing the ionospheric potential resulting from constant current dipole source. In general, any current dipole above the mountain produces higher ionospheric potential as the slope of the curve in Figure 4 labeled "ECM without mountain" is steeper than the slope of the curve labeled "ECM with mountain." Next we discuss the effects of radon emanation [*Baumgaertner et al.*, 2013], corona discharges [*Bazelyan et al.*, 2014], and the shift of the source current in horizontal direction on the ionospheric potential. The effect of radon emanation and corona discharges from a mountain leads to an increase of conductivity above the mountain. That decreases the resistance $R_{s,0-TIB}$ in equation (26) and leads to an increase of ionospheric potential similarly to effects produced by a mountain.

The shift of charge in horizontal direction far away from the mountain leads to a decrease of the ionospheric potential to the value obtained without a mountain. We performed a test determining the dependence of source distance from a mountain on ionospheric potential. We are constrained by symmetry in our simulation, and therefore, the following test within CPM was formulated. The charge monopole is placed at height 6 km above the center of the mountain. We have used a mountain with radius $\alpha_m = 20$ km, and we have removed the center of the mountain to create a crater with a radius of 10 km, effectively creating a hollow cylinder mountain. We note that for a monopole at 6 km the increase in U_{IE}/I_s due to the mountain is 25.1%. The increase of U_{IE}/I_s above the hollow cylinder mountain was reduced to 9.7%. If both radii of the hollow cylinder mountain were increased by 10 km to inner radius 20 km and outside radius 30 km, the increase of U_{IE}/I_s was reduced to 2.3%. Therefore, a 20 km distance of source from the mountain leads to results very close to ECM results without mountain.

In [*Jánský and Pasko*, 2014] it was shown that the ionospheric potential due to a sequence of −CG lightning discharges can be represented also by a current dipole. The periodicity of −CG lighting discharges over the whole Earth is approximately 10^{-1} s which is smaller than the typical timescale of modification of ionospheric potential due to one −CG lightning discharge. The current dipole representing the sequence of −CG lightning discharges is composed of a positive current at the altitude of the bottom negative charge center of a thunderstorm and a negative current at the Earth's surface. The ionospheric potential due to the current dipole representing the realistic sequence of −CG lightning discharges (i.e., with above mentioned frequency 10^{-1} s) is smaller in the presence of a mountain than without a mountain as seen in Figure 4.

Slyunyaev et al. [2014] concluded that the horizontal size of the conductivity perturbations has to be bigger than the height of the atmosphere to obtain good quantitative agreement between the equivalent circuit model and the model based on the continuity equation and Poisson's equation. In our simulations the excellent quantitative agreement is obtained even for much smaller horizontal sizes. One can speculate that the height of the atmosphere might be substituted by altitudes more relevant to the calculation of ionospheric potential as what happens above 20 km does not influence ionospheric potential significantly. Then from the presented results we can empirically establish that the ECM is valid for altitudes of source currents smaller than horizontal size of perturbation $h < \alpha_m$.

4.3. Effects of Thunderclouds With Reduced Conductivity

In this section the influence of the reduction of conductivity inside the thundercloud is studied. The schematics is shown in Figure 1b. Point unit charge is instantaneously injected on axis $\theta = 0$ at altitude h_s, and its ionospheric potential impulse response is calculated. The h_s is varied in the range from 0 to 15.5 km. Then time integral of impulse response M_{IE}^{IR} representing the CPM results of U_{IE}/I_s is compared with that of ECM results from equation (18). Two ECM results are presented in Figure 5, one for a single thundercloud with reduced conductivity σ'' labeled "ECM with cloud" and the second without reduction of conductivity labeled "ECM without cloud." The thundercloud in this example is set between 2.5 km and 12.5 km. The radius of the thundercloud α_c varies from 5 to 20 km, and the conductivity is reduced by a factor of 20.

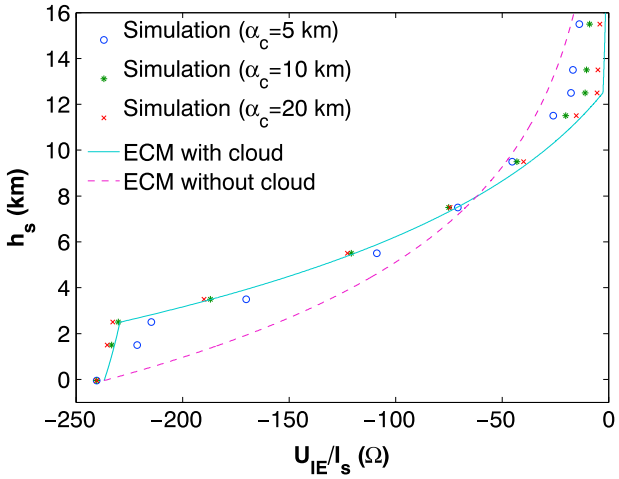

Figure 5. The CPM simulation results of U_{IE}/I_s as a function of source altitude h_s is plotted for three different thundercloud radii: $\alpha_c = 5$ km, 10 km, and 20 km. The cloud bottom boundary is at 2.5 km, and the top boundary is at 12.5 km. The ECM results with reduction of conductivity in the cloud are obtained from equation (18) and are plotted using a solid line, and the ECM results for unperturbed exponential conductivity (ECM without cloud) are plotted using a dashed line.

Figure 5 shows the CPM simulation results of U_{IE}/I_s for three different radii of the thundercloud and ECM results from equation (18) as a function of source altitude h_s. It is seen that for thunderclouds with radii 20 km and 10 km, the ECM results give excellent agreement for source altitudes below 8 km and very good agreement above. The U_{IE}/I_s for the thundercloud with radius 5 km does not give good quantitative agreement with ECM. *Slyunyaev et al.* [2014] used in their work the horizontal size of thunderclouds approximately 5 km and reported significant disagreement with electric circuit model. Our results agree with *Slyunyaev et al.* [2014] for such small horizontal sizes. It is interesting to note that ECM and numerical results cross each other around 8 km. It means that for low-altitude monopole sources the reduction of conductivity enhances their contribution to the ionospheric potential but decreases their contribution for higher altitudes. This effect could be understood in terms of formation of screening charges [*Riousset et al.*, 2010]. In case of source charges close to the top boundary the screening charges are mostly located at the top boundary of the thundercloud. This region has the shortest dielectric relaxation time, and therefore, the ionospheric potential relaxes faster, resulting in smaller M_{IE}^{IR}. Opposite is true for a source at lower altitude where most of the screening charge is located at the bottom thundercloud boundary. The longer relaxation time in this region leads to the larger M_{IE}^{IR} values.

Similarly to the end of the section 4.2, we present a comparison of ECM and simulation results for the case of source current dipole ($I_s = 1$ A placed at altitude $h_{TP} = 9.5$ km and $-I_s$ at $h_{BN} = 5.5$ km). In the case with no reduction of conductivity, equation (13) can be directly used to obtain $U_{IE} = 45.7$ V, valid for both ECM and CPM. In the case with a reduction of conductivity, the $U_{IE,ECM}$ has to be formed from a linear combination of two equations (18) for monopoles at h_{BN} and h_{TP}. The final form gives

$$U_{IE,ECM} = I_s \frac{R_{s,BN-TP}}{R_{s,0-TIB}} R_{atm} = 82.4\,\mathrm{V}, \tag{28}$$

where $R_{s,BN-TP}$ and $R_{s,0-TIB}$ correspond to resistances in source column between the altitudes of bottom negative and top positive charges, and between the Earth and the top ionospheric boundary, respectively. Both resistances are modified by reduction of conductivity inside the thundercloud. The quantity R_{atm} corresponds to the resistance of the whole atmosphere. The CPM results are read from Figure 5 following a procedure described in section 4.2. The ionospheric potential from CPM is then 82.7 V (difference of 0.3% with respect to ECM) for the thundercloud with radius 20 km. The thundercloud with radius 10 km gives 77.7 V (difference of 5.6%), and the thundercloud with radius 5 km gives 63.6 V (difference of 22.8%). The ECM and CPM are again in very good agreement, with relative error less than 6%, for thunderclouds of radius 20 km and 10 km. The error by neglecting the conductivity reduction is 80%, but parameterization using ECM from equation (18) gives very good result for thunderclouds of radius 10 km and greater.

The variation of reduction of conductivity inside the thundercloud and its influence on the ionospheric potential was discussed in *Rycroft and Odzimek* [2010, Figure 3] and in *Slyunyaev et al.* [2014, Figure 5]. Both works

calculated their results using equivalent methods, ECM in *Rycroft and Odzimek* [2010] and theoretical analysis shown to be equivalent to ECM in *Slyunyaev et al.* [2014]. Although different structure of source currents is used, the interpretation of results indicates that the 20-fold reduction of conductivity leads to 2–2.5 times increase of ionospheric potential. This agrees reasonably well with our results within the differences expected from different current structures.

To evaluate the contribution of the sequence of −CG lighting discharges, we analyze the behavior of the results in Figure 5 from 0 to 4 km. The difference between U_{IE}/I_s at 2.5 km and 0 km is 7.5 Ω for ECM with reduction of conductivity inside the thundercloud or for wide thunderclouds in CPM. For exponential conductivity this difference is about 10 times greater and is equal to 80.1 Ω. The U_{IE}/I_s difference between 3.5 km and 0 km is still a factor of 2 higher without reduction of conductivity than with reduction. This means that the sequence of −CG lightning discharges and other GEC current sources transporting the charges under the thundercloud contribute much less to the ionospheric potential than was expected from calculations using exponential conductivity.

5. Conclusions

The principal results of this paper are as follows:

1. We have developed a relation of ionospheric potential to the source current and conductivity profile/resistance for horizontally independent conductivity based on a concept of impulse response. The resulting formulae show consistency with the results published by *Kalinin et al.* [2014].
2. We have modeled the transient response of ionospheric potential due to atmospheric ionization changes produced by γ ray bursts and identified timescales of interest (10^{-2}–10^{1} s). Modifications of steady state ionospheric potential are small even for very intense γ ray bursts, and these are very well reproduced by the equivalent circuit model.
3. We have studied the effect of topography on the ionospheric potential by placing a single mountain directly underneath the source charges. The ionospheric potential per unit source current (U_{IE}/I_s) is evaluated from numerical simulations and compared with the equivalent circuit model. It was found that for radius of mountain 20 km and above, the equivalent circuit model gives an excellent agreement and for 10 km the agreement is very good. The presence of a mountain effectively increases the ionospheric potential for a classic source in the GEC represented by a current dipole. On the other hand, the contribution of a sequence of negative cloud-to-ground lightning discharges to the ionospheric potential is reduced.
4. We have studied the influence of reduction of conductivity inside the thundercloud on the ionospheric potential. The ionospheric potential per unit source current (U_{IE}/I_s) is evaluated from numerical simulations and compared with the equivalent circuit model. It is shown that for thunderclouds with radii 20 km and 10 km, the equivalent circuit model gives excellent agreement for source altitudes below 8 km and a very good agreement above. The reduction of conductivity effectively increases the ionospheric potential for a classic source in the GEC represented by a current dipole and reduces the ionospheric potential for a sequence of negative cloud-to-ground lightning discharges.

Acknowledgments
This research was supported by the NSF under grant AGS-1135446 to Penn State University. All data are directly available after a request is made to author J.J. or V.P.P.

References

Baumgaertner, A. J. G., J. P. Thayer, R. R. Neely III, and G. Lucas (2013), Toward a comprehensive global electric circuit model: Atmospheric conductivity and its variability in CESM1(WACCM) model simulations, *J. Geophys. Res. Atmos.*, *118*, 9221–9232, doi:10.1002/jgrd.50725.

Baumgaertner, A. J. G., G. M. Lucas, J. P. Thayer, and S. A. Mallios (2014), On the role of clouds in the fair weather part of the global electric circuit, *Atmos. Chem. Phys.*, *14*(16), 8599–8610, doi:10.5194/acp-14-8599-2014.

Bayona, V., N. Flyer, A. J. G. Baumgaertner, and G. M. Lucas (2015), A 3-D RBF-FD elliptic solver for irregular boundaries: Modeling the atmospheric global electric circuit with topography, *Geosci. Model Dev. Discuss.*, *8*, 3523–3564, doi:10.5194/gmdd-8-3523-2015.

Bazelyan, E. M., Y. P. Raizer, and N. L. Aleksandrov (2014), Non-stationary corona around multi-point system in atmospheric electric field: I. Onset electric field and discharge current, *J. Atmos. Sol. Terr. Phys.*, *109*, 80–90, doi:10.1016/j.jastp.2013.03.029.

Browning, G. L., I. Tzur, and R. G. Roble (1987), A global time-dependent model of thunderstorm electricity. 1. Mathematical properties of the physical and numerical models, *J. Atmos. Sci.*, *44*(15), 2166–2177, doi:10.1175/1520-0469(1987)044<2166:AGTDMO>2.0.CO;2.

Dejnakarintra, M., and C. G. Park (1974), Lightning-induced electric-fields in ionosphere, *J. Geophys. Res.*, *79*(13), 1903–1910, doi:10.1029/JA079i013p01903.

Hays, P., and R. Roble (1979), Quasi-static model of global atmospheric electricity. 1. Lower atmosphere, *J. Geophys. Res.*, *84*(NA7), 3291–3305, doi:10.1029/JA084iA07p03291.

Holzer, R., and D. Saxon (1952), Distribution of electrical conduction currents in the vicinity of thunderstorms, *J. Geophys. Res.*, *57*, 207–216, doi:10.1029/JZ057i002p00207.

Inan, U. S., N. G. Lehtinen, R. C. Moore, K. Hurley, S. Boggs, D. M. Smith, and G. J. Fishman (2007), Massive disturbance of the daytime lower ionosphere by the giant γ-ray flare from magnetar SGR 1806-20, *Geophys. Res. Lett.*, *34*, L08103, doi:10.1029/2006GL029145.

Jánský, J., and V. P. Pasko (2014), Charge balance and ionospheric potential dynamics in time-dependent global electric circuit model, *J. Geophys. Res. Space Physics*, *119*(12), 10,184–10,203, doi:10.1002/2014JA020326.

Kalinin, A. V., N. N. Slyunyaev, E. A. Mareev, and A. A. Zhidkov (2014), Stationary and nonstationary models of the global electric circuit: Well-posedness, analytical relations, and numerical implementation, *Izv. Atmos. Ocean. Phys.*, *50*(3), 314–322, doi:10.1134/S0001433814030074.

Lyons, R. (1997), *Understanding Digital Signal Processing*, Addison Wesley Longman, Inc., Reading, Mass.

Makino, M., and T. Ogawa (1984), Responses of atmospheric electric field and air-earth current to variations of conductivity profiles, *J. Atmos. Terr. Phys.*, *46*(5), 431–445, doi:10.1016/0021-9169(84)90087-4.

Price, C., and V. Mushtak (2001), The impact of the August 27, 1998, γ-ray burst on the Schumann resonances, *J. Atmos. Sol. Terr. Phys.*, *63*, 1043–1047, doi:10.1016/S1364-6826(01)00014-1.

Pruppacher, H. R., and J. D. Klett (1997), *Microphysics of Clouds and Precipitation*, 2nd ed., Kluwer, Netherlands.

Riousset, J. A., V. P. Pasko, P. R. Krehbiel, W. Rison, and M. A. Stanley (2010), Modeling of thundercloud screening charges: Implications for blue and gigantic jets, *J. Geophys. Res.*, *115*, A00E10, doi:10.1029/2009JA014286.

Rycroft, M. J., and R. G. Harrison (2012), Electromagnetic atmosphere-plasma coupling: The global atmospheric electric circuit, *Space Sci. Rev.*, *168*, 363–384, doi:10.1007/s11214-011-9830-8.

Rycroft, M. J., and A. Odzimek (2010), Effects of lightning and sprites on the ionospheric potential, and threshold effects on sprite initiation, obtained using an analog model of the global atmospheric electric circuit, *J. Geophys. Res.*, *115*, A00E37, doi:10.1029/2009JA014758.

Rycroft, M. J., A. Odzimek, N. F. Arnold, M. Fullekrug, A. Kulak, and T. Neubert (2007), New model simulations of the global atmospheric electric circuit driven by thunderstorms and electrified shower clouds: The roles of lightning and sprites, *J. Atmos. Sol. Terr. Phys.*, *69*(17–18), 2485–2509, doi:10.1016/j.jastp.2007.09.004.

Slyunyaev, N. N., E. A. Mareev, A. V. Kalinin, and A. A. Zhidkov (2014), Influence of large-scale conductivity inhomogeneities in the atmosphere on the global electric circuit, *J. Atmos. Sci.*, *71*(11), 4382–4396, doi:10.1175/JAS-D-14-0001.1.

Stansbery, E. K., A. A. Few, and P. B. Geis (1993), A global model of thunderstorm electricity, *J. Geophys. Res.*, *98*(D9), 16,591–16,603, doi:10.1029/93JD01356.

Tinsley, B. A., and L. Zhou (2006), Initial results of a global circuit model with variable stratospheric and tropospheric aerosols, *J. Geophys. Res.*, *111*, D16205, doi:10.1029/2005JD006988.

Tzur, I., and R. Roble (1985), The interaction of a dipolar thunderstorm with its global electrical environment, *J. Geophys. Res.*, *90*(ND4), 5989–5999, doi:10.1029/JD090iD04p05989.

Williams, E., and E. Mareev (2014), Recent progress on the global electrical circuit, *Atmos. Res.*, *135*, 208–227, doi:10.1016/j.atmosres.2013.05.015.

Zhou, L., and B. A. Tinsley (2010), Global circuit model with clouds, *J. Atmos. Sci.*, *67*, 1143–1156, doi:10.1175/2009JAS3208.1.